MATERIALS SCIENCE

3D printing of nanowrinkled architectures via laser direct assembly

Xuhao Fan[1], Chunsan Deng[1], Hui Gao[1,2], Binzhang Jiao[1], Yuncheng Liu[1], Fayu Chen[1], Leimin Deng[1,2], Wei Xiong[1,2]*

Structural wrinkles in nature have been widely imitated to enhance the surface functionalities of objects, especially three-dimensional (3D) architectured wrinkles, holding promise for emerging applications in mechanical, electrical, and biological processes. However, the fabrication of user-defined 3D nanowrinkled architectures is a long-pending challenge. Here, we propose a bottom-up laser direct assembly strategy to fabricate multidimensional nanowrinkled architectures in a single-material one-step process. Through the introduction of laser-induced thermal transition into a 3D nanoprinting process for leading the point-by-point nanoscale wrinkling and the self-organization of wrinkle structures, we have demonstrated the program-controlled and on-demand fabrication of multidimensional nanowrinkled structures. Moreover, the precise control of wrinkle morphology with an optimal wavelength of 40 nanometers and the regulation of the dynamic transformation of wrinkled cellular microstructures via interfacial stress mismatch engineering have been achieved. This study provides a universal protocol for constructing nearly arbitrary nanowrinkled architectures and facilitates a new paradigm in nanostructure manufacturing.

INTRODUCTION

The ubiquitous wrinkle structures in nature endow biological surfaces with enhanced functionalities beyond their three-dimensional (3D) shape features, such as the superior deformability of the cell membrane (*1*), the rapid superspreading property of animal corneas (*2*), and the increased intellectual capacities allowed by brain gyrification (*3*). These natural surface patterns have inspired artificial multiscale structures with distinctive design mentalities and have attracted extensive research attention for various applications, including soft electronics (*4*, *5*), smart displays (*6*, *7*), surface engineering (*8*, *9*), and cell culture (*10*, *11*). To fabricate wrinkles with the desired structure, researchers have developed multiple manufacturing methods through the strategy of introducing surface instability, such as thermal shrinkage (*12*, *13*), prestretching release (*14*, *15*), mechanical compression (*16*, *17*), and solvent swelling (*18*, *19*). Diverse wrinkle patterns have been constructed and have exhibited extraordinary properties for anticounterfeiting (*20*, *21*), flexible sensors (*22*, *23*), and tissue engineering applications (*24*, *25*). In addition to these wrinkles on planar surfaces, the ongoing technical evolution for advanced applications, such as artificial organ 3D printing (*26*, *27*), ultrasensitive detectors (*28*, *29*), or ultrahigh-capacity energy storage devices (*30*) with large surface-to-volume ratios, all call for the extension of wrinkled structures from 2D space to higher dimensionality (*31*), which is expected to further enhance the functionality of devices.

In the pursuit of achieving 3D wrinkled structures, substantial efforts have been devoted to investigating biological wrinkles and bionic wrinkling construction on nonplanar substrates (*32*). Wrinkling patterns on curved substrates, such as spheres (*33*), cylinders (*12*), and tubes (*34*), have been fabricated by constructing core-shell systems with mismatch modulus and then by triggering surface instability under external stimuli. However, these methods can only achieve an intrinsic wrinkling pattern that is strongly constrained by the geometry of the substrate, which cannot be applied to arbitrary architectures. Although approaches using laser path guiding (*35*–*37*), light-induced patterning (*20*, *38*), and nonuniform polymerization (*39*) have been developed to realize the wrinkle formation of designed 2D patterns, these techniques still suffer from limited 3D structuring (*40*). Therefore, a long-pending challenge still exists for manufacturing 3D wrinkled structures with superior designability for desired architectures and strong controllability of wrinkle geometry.

Here, we report an ultrafast laser-induced assembly method to directly print nanowrinkled architectures with ultrahigh spatial resolution and nearly arbitrary 3D structuring capacity. The template-free 3D fabrication of wrinkled architectures is realized. This technique features the coupling of the laser-induced thermal responsiveness of hydrogels with a nanoprinting process, which guides the self-organization of nanowrinkles and the multidimensional structuring. During the entire wrinkling process, only one step of femtosecond laser direct writing (FsLDW) in a single hydrogel precursor material is involved. This bottom-up fabrication demonstrates a flexible ability to construct wrinkle patterns into 1D, 2D, and 3D hierarchical architectures. Furthermore, we realize the precise control and tunability of wrinkle pattern formation and observe an interesting yet abnormal micromechanical behavior of the as-fabricated 3D wrinkled microarchitecture. Furthermore, by introducing structural stress mismatch, we realize the dynamic regulation of honeycomb microstructures from surface wrinkling to structural transformation. This bottom-up laser-induced 3D assembly method shares the similarity and merits of the natural formation of wrinkled structures during a biological growth process and builds a multifunctional platform for the construction of various sophisticated wrinkle architectures for multiple applications.

RESULTS

Design of nanoscale wrinkling

To reach the threshold of two-photon absorption (TPA), a femtosecond laser is commonly used and tightly focused using a high numerical aperture (NA) objective (*41*). As a side effect, the focal

[1]Wuhan National Laboratory for Optoelectronics and School of Optical and Electronic Information, Huazhong University of Science and Technology, Wuhan 430074, China. [2]Optics Valley Laboratory, Wuhan, Hubei 430074, China.
*Corresponding author. Email: weixiong@hust.edu.cn

temperature in water increases with the deposited energy due to the photothermal effect. Benefiting from an ultrashort pulse, a femtosecond laser can effectively suppress the heat-affected zone (*42*–*44*). Thus, an increase in temperature occurs only at the focus spot and can dissipate quickly upon the removal of the laser radiation. With the switching and scanning of the ultrafast laser beam, the laser focal spot can be used as a localized heating source in a solution (*45*, *46*). However, this additional capability of a focused laser is considered to have a negative impact on the accuracy in previous FsLDW works. Here, we propose a temperature-responsive hydrogel precursor to use laser-induced heat stimulation for nanoscale wrinkling. Figure 1 summarizes the strategy for nanoscale wrinkling and structural construction.

A poly(ethylene glycol) diacrylate (PEGDA)–based hydrogel is used because of its inherently low photopolymerization threshold and exceptional biocompatibility (*47*). *N*-isopropyl acrylamide (NIPAM) is added as a functional monomer, which can form a cross-linked network with PEGDA via two-photon polymerization (TPP) (fig. S1). NIPAM is a temperature-responsive hydrogel, with the concurrent presence of amide groups and isopropyl groups in the side chain, in which the amide group is hydrophilic while the isopropyl group is hydrophobic, resulting in a temperature-induced volume phase transition of poly(NIPAM) (PNIPAM) at approximately 32°C (*48*). Ethylene glycol (EG), as an additive, creates an environment for hydrophilic groups to form hydrogen bonds while enhancing the mutual solubility of the components in the solution. By theoretical calculation, the focal temperature is in the range of 40° to 70°C in this hydrogel precursor under different processing parameters (see note S1 for detailed calculation), which is above the lower critical solution temperature (LCST) of NIPAM. Thus, a responsive volume change of the fabricated hydrogel microstructure is expected (fig. S2 and movie S1).

During the FsLDW process, the focal spot of the laser is steered by a pair of galvo mirrors and a piezoelectric nanostage for high-speed 2D scanning and high-resolution step movements, respectively (Fig. 1A). Oligomers that undergo the exposure exceeding the TPA threshold dose (typically 5 to 10 mW of laser power) are transformed into a polymer network via photoinduced cross-linking, leading to a volume element "voxel" (Fig. 1B). Voxel lines composed of voxels are formed along with the scanning of the laser focal point. In general,

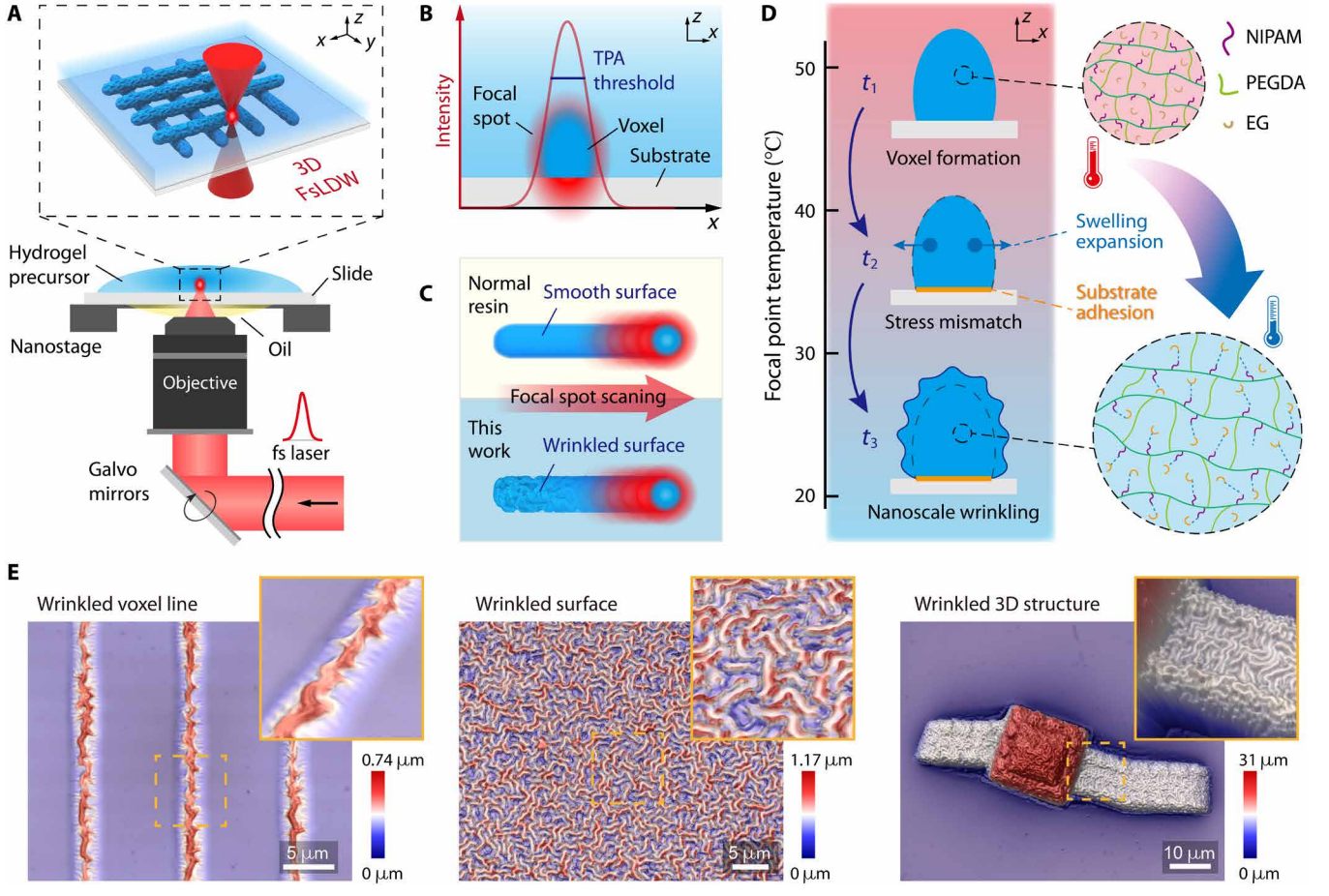

Fig. 1. Strategy for nanoscale wrinkling. (**A**) Schematic illustration of the fabrication setup and the formation of wrinkled voxel lines along with the laser scanning pathway. Zoomed-in schematic of the as-written voxel lines shows the nanoscale wrinkling phenomenon and the 3D structuring capability of FsLDW. (**B**) The calculated light intensity distribution of a typical focal spot. (**C**) Comparison diagram of surface morphology between normal acrylic resin and hydrogel precursor in this work. (**D**) Diagrammatic sketch of the expansion-induced stress mismatch between the voxel and rigid substrate. The focal temperature is above the LCST of the material, and with laser scanning, the polymerized hydrogels change from hydrophobic to hydrophilic and, thus, expand in volume. The stress mismatch induced by swelling expansion and substrate adhesion contributes to the nanoscale wrinkling. (**E**) Wrinkled microarchitectures from 1D voxel line to 2D plane and 3D structure (a "Great Wall" model).

high surface smoothness can be realized by taking advantage of the self-smoothing effect in widely used acrylic resins (Fig. 1C). However, for the hydrogel precursor in this work, the increase in the local temperature under laser radiation leads to the predominance of hydrophobic isopropyl groups in the cross-linking network during voxel formation. Upon the removal of the laser spot, which results in temperature reduction, the hydrophilic amide group becomes dominant in the as-formed voxel and leads to the formation of a hydrogen bond between EG and the hydrogel network. As a result, the voxel that is photopolymerized at a slightly elevated temperature swells with the removal of the laser spot due to the temperature-induced volume phase transition of PNIPAM (Fig. 1D). The volume expansion of the voxel and the restriction of the rigid substrate contribute to the stress mismatch at the interface, which triggers the wrinkling of the voxel (see note S2 for a detailed analysis). With the scanning of the focal spot, an effective response of wrinkling is expected, and the surface morphology of the microgel structure presents an apparent wrinkled structure compared to that of the standard acrylic resin (fig. S3). The 3D laser scanning confocal microscope (3D LSCM) images (Fig. 1E and fig. S4B), scanning electron microscopy (SEM) images (fig. S4A), and atomic force microscope (AFM) images (fig. S4E) are consistent with the proposed wrinkling strategy. The optimal wrinkle wavelength is found to be smaller than 40 nm (see the 'Regulation of wrinkle morphology' section); as a comparison, the finest spatial voxel line width is found to be approximately 400 nm (fig. S5), demonstrating that the thermal coupling process plays a key role in the improved wrinkle characteristics, in addition to the high-resolution feature of TPP.

In the FsLDW process, the polymerized microgel is sensitive to the precursor material composition. Thus, the ratio of monomer to cross-linker, as well as the laser processing parameters, is optimized to yield a thermal-sensitive microgel that can satisfy the stress mismatch conditions corresponding to the wrinkling process. Experimentally, the use of EG to replace water reduces the swelling ratio of the microgel and enables the structure to remain on the substrate (fig. S6 and movie S2). Under a comprehensive consideration of solubility and processability, the concentrations of NIPAM in the hydrogel precursor were optimized to 23% (w/w). The successful reactions of both PEGDA-NIPAM copolymerization and PEGDA self-polymerization were confirmed by the Fourier transform infrared spectroscopy (FTIR) spectra (fig. S7). For the positive correlation between responsive swelling expansion and exposure dose of laser, high laser power or low scanning velocity during fabrication will lead to the separation of the hydrogel sheet from the substrate (fig. S8). To improve the interfacial adhesion, we treated the glass substrates with oxygen plasma and chemical immersion before use (see Materials and Methods) (*49*). The enhanced interfacial adhesion promotes in situ stress mismatch during laser processing, and under a few extreme conditions, the formation of wrinkles on microstructures can be directly observed in real time (fig. S9 and movie S3), indicating that the wrinkles are in situ formed during the laser processing. Meanwhile, parameter regions for wrinkle 3D printing were mapped out through parameter sweep, and the prepared hydrogel precursor was prototyped into various microscale 3D geometries according to the optimized parameters, demonstrating excellent structural ability (fig. S10 and movie S4). Furthermore, comparative experiments via temperature-controlled polymerization demonstrated the concept that thermal transition leads to volume change during the FsLDW process (fig. S11 and movie S5). Morphology characterizations of nanowrinkled architectures ruled out the potential influence of a thin Au layer sputtered before SEM tests (fig. S12).

Structural construction of nanowrinkles

In TPP lithography, the scanning of the laser focus according to the designed 3D patterns yields the desired 3D microstructure. Similarly, a wrinkled voxel line can be achieved through FsLDW in the hydrogel precursor. With the reduction of the scanning pitch, the overlapping exposure induces the self-organization of hydrogel voxels (Fig. 2A), leading to the generation of a uniformly disordered wrinkling surface without the trace of scanning lines. Unlike the sharp boundary of two neighboring voxels in the polymerization of widely used acrylic resins, the self-organization of nanowrinkles smooths the scanning trace of point-by-point laser direct writing, contributing to the well 3D forming ability of wrinkle 3D printing. Specifically, this progress involves the exact cooperation between the laser processing parameters and microgel swelling. For the Gaussian profile of the laser beam, laser scanning cannot induce the complete polymerization and cross-linking of monomers in the precursor, resulting in inhomogeneous hydrogel lines with greater cross-linking at the interior and less cross-linking at the periphery. When the pitch between parallel voxel lines is less than the wavelength, the monomers in the overlapping area of laser scanning polymerize under multiple repeated exposures (Fig. 2B and fig. S13). Two typical surface morphologies are shown in Fig. 2C. Connections between voxel lines can be observed because of the proliferation of radical polymerization. With a further decline in line pitch, the voxel line path is concealed beneath the self-organized wrinkling surface. The evolution of wrinkle morphology between parallel voxel lines under gradient line pitch is shown in Fig. 2D. The surface wrinkle pattern remains with a uniform wavelength when the line pitch is less than 1 μm and shows a clear correlation to the overlapping exposure area. Furthermore, the self-organization of voxel lines can be extended to layer-by-layer construction (Fig. 2, E and F). By matching the slice parameters, we prepared a series of planar geometry patterns with nanowrinkled surfaces (Fig. 2, G and H, and fig. S14).

Benefiting from the direct writing feature of FsLDW, the on-demand fabrication of architectures with complex geometries varying from 2D to 3D is realized by introducing designable scanning paths. Circular, hexagonal, square, and triangular grid patterns with nanowrinkles are successfully fabricated (Fig. 3A and fig. S15). The side length of the unit structure is 3 to 5 μm, and the cross-sectional width is 1 μm. The pitch of parallel voxel lines is 300 nm. Four to six layers are scanned with a layer distance of 500 nm on a rigid substrate. Meanwhile, an array of microbricks with nanowrinkles is fabricated in a programmable manner, which shows a large surface-to-volume ratio (Fig. 3B). With the help of computer-aided design, the scanning path of different layers can be contrived to prepare wrinkle patterns with higher dimensional information, such as patterned wrinkles (Fig. 3C) and hierarchical wrinkles (Fig. 3D and fig. S16). Furthermore, because of the template-free capability, excellent geometric designability, and nanoscale spatial resolution of this method, the whole 3D structure can be polymerized by 3D FsLDW according to the predesigned scanning paths, and an actual 3D microarchitecture with nanowrinkles is fabricated. Various 3D models are made, such as the Thinker (Fig. 3E), a human head (Fig. 3F), the Great Wall of China (Fig. 3G), and a human brain (Fig. 3H). To the best of our knowledge, this is the first study to achieve these complex nanowrinkled 3D architectures via a single-material one-step process.

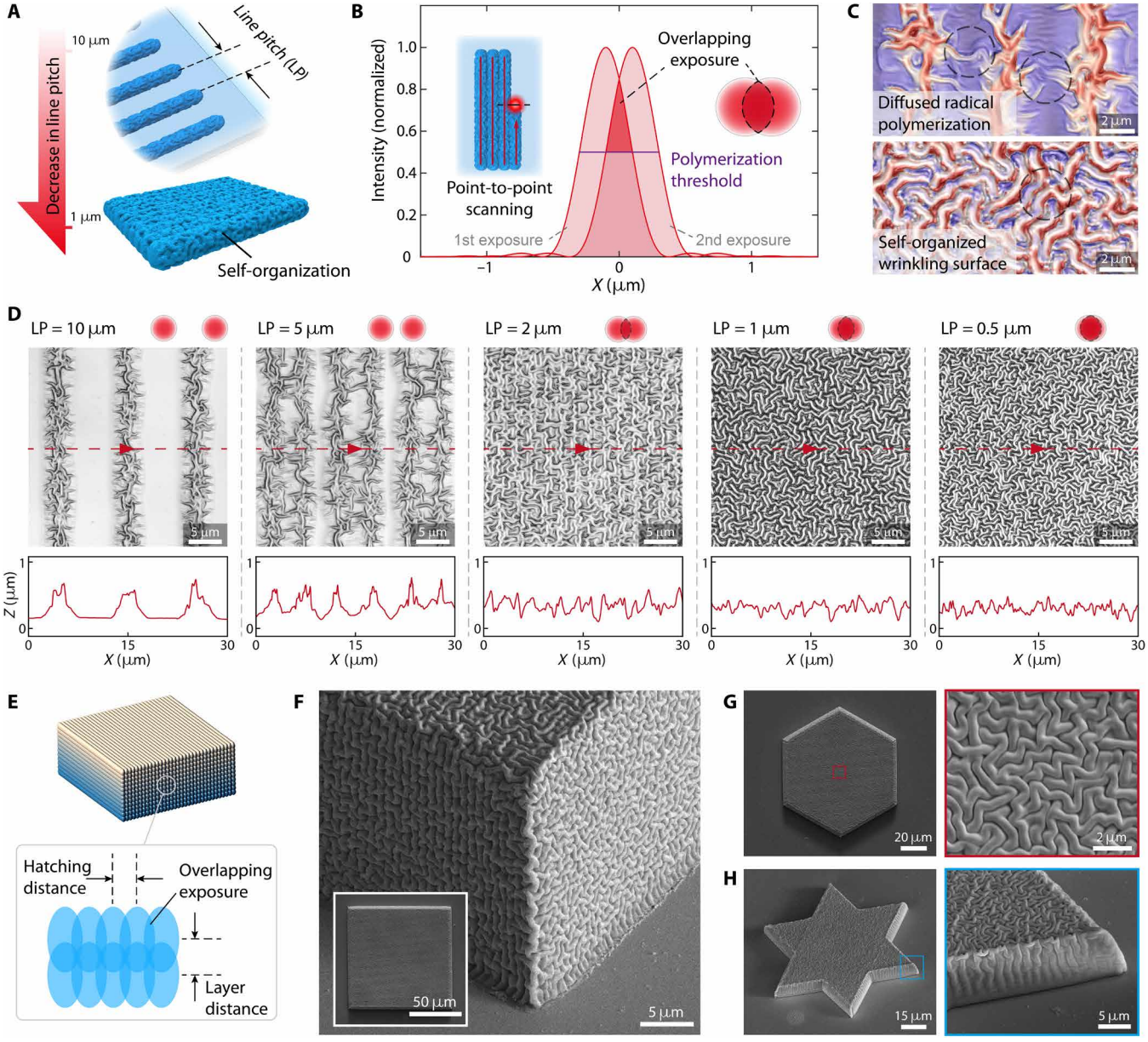

Fig. 2. Self-organization of wrinkle structures. (**A**) Schematic of the self-organization process. (**B**) The overlapping exposure area during point-by-point scanning with a line pitch of 1 μm. (**C**) 3D LSCM images of self-organized structures induced by overlapping exposure. The curing thickness of the voxel line is tuned to approximately 300 nm by controlling the lowered depth of the focal spot. (**D**) 3D LSCM images and the curves for positions are marked. The line pitch ranges from 10 to 0.5 μm. The decrease in line pitch increases the overlapping exposure area, leading to the weak cross-linked hydrogel as a homogeneous wrinkled surface. (**E**) Schematic of the cuboid scanning path and the corresponding slice parameters. Two variable parameters related to the scanning path are identified: hatching distance (d_h) and layer distance (d_l). The overlapping area of exposure is marked. (**F**) Tilted views of the nanowrinkled cuboid. The inset at the bottom left is the top view image of the cuboid structure with wrinkled surfaces. (**G** and **H**) Nanowrinkled planar geometry structure with zoomed-in views of surface morphology.

Regulation of wrinkle morphology

As a substantial demand for applications, adjustable wrinkle morphology is vital for increasing the applicability of wrinkle 3D printing. The merit of variable parameters made FsLDW an excellent technique for the regulation of wrinkle morphology. Because of the coupling effect of polymerization and swelling-induced instability, the nanoscale wrinkling and self-organization of microgels involve the transfer of matter and energy at the same time. As a result, the processing parameters have a notable influence on the self-organized wrinkle morphology (note S3). Using a simplified exposure model (*50*, *51*), we explored the relations between processing parameters and wrinkle characteristics by changing the laser power (P) only. The density of the wrinkled structures gradually increases as P changes from 10 to 50 mW using the same scanning velocity (v) and path (Fig. 4A). Through digital image processing (fig. S14), we analyzed the characteristics of wrinkle patterns and found that the wrinkle wavelength (λ) is largely insensitive to the applied FsLDW process parameters, typically P. As shown in Fig. 4B, the maximum wrinkle

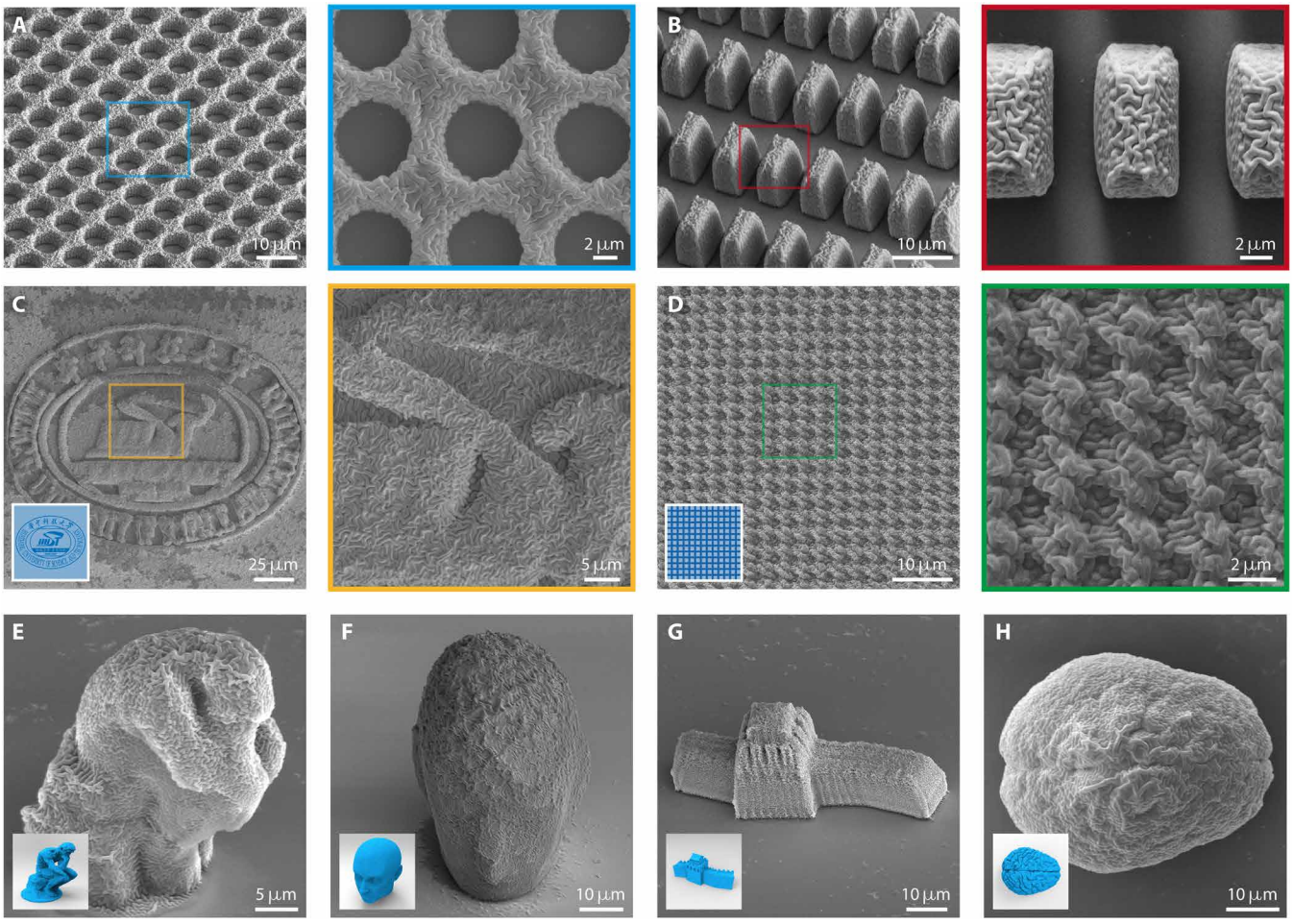

Fig. 3. Printing of complex nanowrinkled 2D and 3D microarchitectures. (**A**) SEM images of circular nanowrinkled grid structures with zoomed-in views of surface morphology. (**B**) SEM images of microbricks with nanowrinkles (length = 5 μm, width = 2 μm, and height = 8 μm). (**C**) The nanowrinkled pattern of the Huazhong University of Science and Technology emblem. (**D**) SEM images of hierarchical wrinkles on a planar rigid substrate. (**E** to **H**) SEM images of 3D microarchitectures with nanowrinkles.

wavelength is approximately 75 to 80 nm with P = 10 mW and v = 5 mm s^{-1}, where the degree of polymerizing conversion starts to meet the requirement for forming a cuboid. With P increasing from 10 to 40 mW, λ decreases accordingly, with an almost linear downward trend. For P > 40 mW, λ plateaus at approximately 40 nm and is almost 50% for P = 10 mW. Thus, 40 nm is the optimal λ for topologically disordered wrinkled morphologies. It is demonstrated that the typical λ of disordered wrinkled surfaces ranges from 40 to 80 nm and can be flexibly regulated by tuning the processing laser power. Meanwhile, the evolution of wrinkle morphology on 3D wrinkled architectures displays a consistent trend with the proposed regulation process using laser power modulation (fig. S18). In this way, the in situ controllable features significantly reduced the regulating costs and improved the designability.

To explore how nanowrinkles affect the properties of 3D nanowrinkled microstructures, we conducted a micromechanical characterization of 3D printed structures with compression and lateral testing modes (see Materials and Methods and figs. S19 and S20). We printed a series of microcuboids with a gradual increase in laser power from 10 to 50 mW at a constant scanning speed of 15 mm s^{-1} (Fig. 4C). We characterized the mechanical properties of the hydrogel microcuboids under compression test mode and measured the stiffness values of the printed samples at different laser powers in the FsLDW process (Fig. 4D). When the laser power is 10 mW, the wavelength of the wrinkle pattern is approximately 75 nm, and the corresponding sample has a stiffness of 25,000 N m^{-1}. When the laser power is 50 mW, the stiffness of the sample is stable at 3000 N m^{-1}. Moreover, we measured the adhesive forces using a lateral microforce sensing probe (fig. S20). We obtained a maximum measured adhesive force of 326.1 μN in the microcuboid fabricated with P = 40 mW, while the microcuboid fabricated with P = 20 mW shows an elastic deformation curve within the sensor range. The adhesive results indicate the decrease in adhesion energy with laser power. As a result, the mechanical influence of the nanowrinkles on the cuboid architecture was established via micromechanical characterization.

In general, the mechanical properties of polymerized structures are related to the extent of cross-linking between polymer chains, which correlates with the exposure dose. For example, laser power shows a significant impact on the mechanical properties of the commercial acrylate-based resin IP-Dip, allowing to increase Young's modulus from 0.6 to 3.6 GPa (*51*). However, abnormal micromechanical behavior is found in the wrinkled cuboids. The samples present lower stiffness, which is the expression of softer mechanical

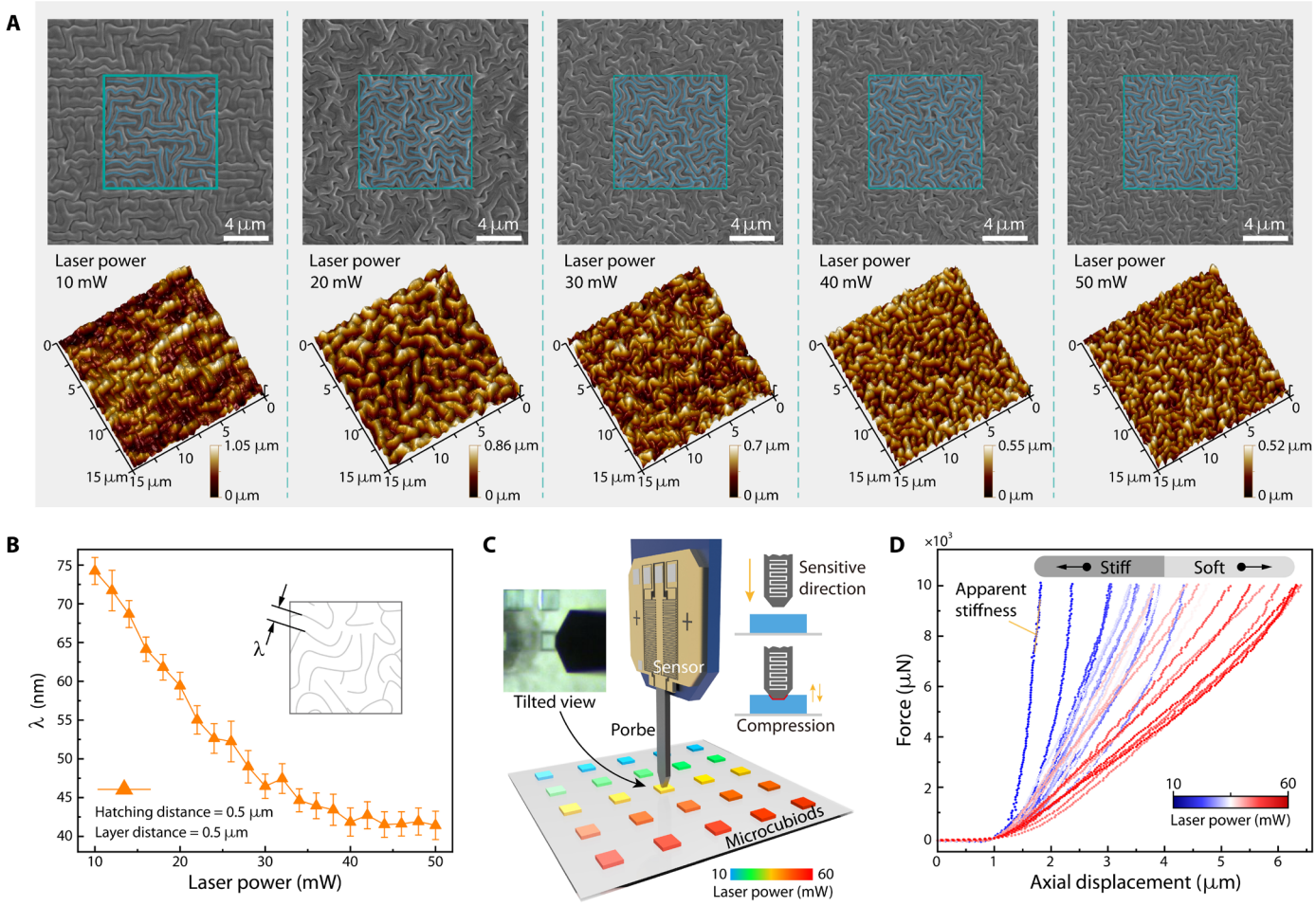

Fig. 4. Adjustable wrinkle morphology and micromechanical property. (**A**) SEM and AFM images of the nanowrinkled surface fabricated using laser power from 10 to 50 mW, with $v = 5$ mm s^{-1} and $d_h = d_l = 500$ nm. (**B**) Statistics of wrinkled surface wavelength for different laser powers. (**C**) Schematic illustration of the micromechanical test of printed samples. The silicon needle tip with a 50 μm–by–50 μm cross section is pushed down vertically onto the top edge of each microcuboid (100 μm by 100 μm by 30 μm) with center alignment to measure the stiffness of the printed gels. The inset depicts the experimental setup. (**D**) Force-displacement curves of TPP-written hydrogel microcuboids on *P* over a range of 10 to 60 mW, with $v = 5$ mm s^{-1} and $d_h = d_l = 500$ nm. Apparent stiffness can be revealed from the loading force-displacement curves during compression, using a linear fit after the precorrection to system deformations.

properties, with an increase in laser power. The existence of wrinkles is believed to be the main reason for this micromechanical anomaly (fig. S19D). As found in the regulation of wrinkle morphology, the wavelength of wrinkle patterns decreased with increasing laser power. When subjected to mechanical compression experiments, microcuboids with smaller wrinkle structures can form more slips within their architecture. This process is similar to the phenomenon of stone and sand compressed by an external force. They are made of the same material, but the slip of the sand makes it easier to change their shape. Although the exact reason for the abnormal mechanical behavior still needs more in-depth investigation, the mechanical influence of the nanowrinkles on architectures is evident, which provides a new way to regulate the mechanical properties of objects.

Biomimetic transformation of cellular structures

From seed germination to maturity and withering, the growth of plants and the generation of surface morphology are correlated, corresponding to the growth stress of each growth state (*52*, *53*). Limited by the formation mechanism, current methods to fabricate wrinkles only provide the intrinsic wrinkling pattern that strongly depends on its original material system and defined design, which lacks spatial variety and is far different from that of the actual physiological processes (*32*). Here, to mimic the bottom-up growth process, FsLDW provides an unprecedented platform for creating architectures with both structural deformation and surface wrinkling. The swelling-induced compressive stress competes with the structure-interface adhesion force. Furthermore, this competition presents a transient equilibrium state during architectural construction and guides the sequential wrinkling and deformation of the hydrogel microstructure.

The juxtaposition of swelling stress and interfacial adhesion force is exhibited during the FsLDW process of hydrogel microarchitectures, and the resulting mechanical instability leads to remarkably different surface topography and deformation states of the solid and hollow units due to the restriction of dimension. For solid units such as cuboids (Fig. 5, A and B), the swelling-induced transient compressive stresses first bring about surface wrinkling under the resistance of interfacial adhesion. When the strains are large enough to

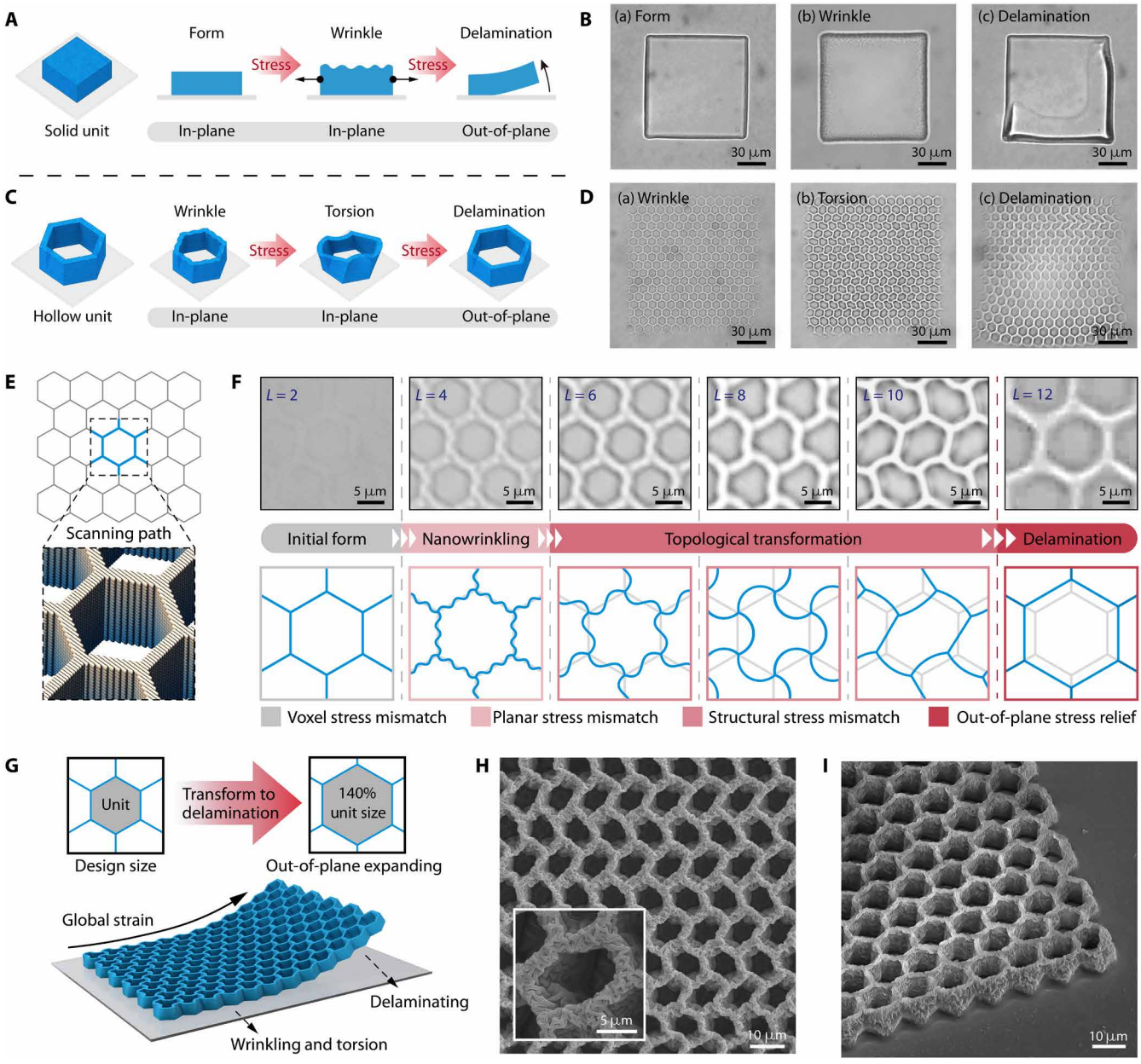

Fig. 5. Transition of wrinkling to deformation and delamination. (**A** and **B**) Illustration and optical micrographs of a solid unit on a rigid substrate undergoing surface wrinkling and delamination in response to swelling stress. (**C** and **D**) Illustration and optical micrographs of surface-attached cellular structures undergoing nanowrinkling, in-plane torsion, and out-of-plane delamination. (**E**) Schematic of a planar hexagonal cellular structure and the scanning path of the FsLDW point-by-point process. (**F**) Optical images and schematic illustration of the microstructures at different states of the global strain. Under the same processing parameters, the stress mismatch state corresponds to the number of scanning layers (*L*). (**G**) Illustration of deformation-to-delamination transition in cellular microstructures under the rise of global stress. The unit size is expanded to 140% of the design size after undergoing the transition from wrinkling to deformation and delamination. (**H**) Top view of the deformed hexagonal microcellular structure, imaged using a scanning electron microscope. The inset at the bottom left is the zoomed-in image of the hexagonal hollow unit with both surface nanowrinkles and shape torsion. (**I**) Tilt view of the surface-attached cellular microstructures deforming into achiral configuration.

overcome the film-substrate interfacial adhesion, a hydrogel microcuboid on the glass substrate will undergo the transition from surface wrinkling to a delaminated state (fig. S21 and movie S6) (*54*). Two classes of mechanical instability behavior can be observed: wrinkling and delamination. For hollow units such as honeycomb (Fig. 5, C and D), the compressive stress is subject to each element and then induces the structured stress mismatch in the cellular microstructure. The bottom of the microstructure is fixed on the rigid substrate, and the surface of the microstructure wrinkles when the stress gradient is slight. As the stress increases, the hanging layer undergoes a transition from wrinkling to deformation due to an expansion effect (fig. S22 and movie S7).

The scanning path of hexagonal cellular structures during the FsLDW process is shown as an example (Fig. 5E). The side length

and width of the hexagonal unit are 5 and 1 μm, respectively. During the layer-by-layer processing, the initial layers were formed in a unit structure and kept in constant shape with the designed pattern (Fig. 5F). The hydrogel cellular structures were attached to a rigid glass substrate through the adhesion energy between the structure and substrate. Surface wrinkling occurs when the hexagonal cellular structures remain attached to the substrate and suffer the combined action of the swelling-induced transient compressive stresses and the resistance of interfacial adhesion. As the height of structures synchronously increases with the scanning layer, the combined action of swelling structural stress and adhesion energy incites mechanical instability in the cellular microstructures, resulting in in-plane transformations to accommodate the strain energy in the system. The competitive relationship between structural stress and interfacial adhesion can be regulated by the number of scanning layers. By regulating the strain energy of the system, when strains are high enough to overcome the interfacial adhesion, cellular microstructures detach from the substrate along with the maximum strain position (Fig. 5G and fig. S23). The cellular microstructures with characteristics of both wrinkles and torsional deformation demonstrate an excellent retention ability and a high repeatability for the laser direct assembly process (Fig. 5, H and I). Furthermore, the dynamic evolution process from wrinkling to torsion and delamination can be observed in real time and can be precisely regulated and is highly consistent with the simulation results (fig. S24), which indicates that this biological manufacturing process can be realized for various structures through computer-aided design (fig. S25 and movie S8).

This bionic manufacturing process in which the external coupling field acts on the 3D structuring process enables the printed structure to have the characteristics of both topological transformation and surface morphology regulation. As an additive manufacturing process that imitates biological growing stress, this approach is promising for extending wrinkle applications from 3D to 4D. For example, scaffolds that are capable of adapting to cell changes can be used to simulate the natural cellular environment in live organisms and tailor dynamic environments for the study of single cells and tissues (*10*, *11*). In addition, using FsLDW to trigger the topological transformation of cellular structures can produce a variety of chiral and achiral metamaterials (*55*), which are useful for acoustic and light wave modulation (*56*) in various potential applications.

DISCUSSION

In summary, we developed a wrinkle 3D printing methodology using a thermally responsive hydrogel precursor via maskless FsLDW. Using the laser-induced thermal transition, we demonstrated the proof-of-concept studies via nanoscale wrinkling of hydrogel voxels and self-organized formation of topological wrinkled surface morphologies. Exerting the merits of FsLDW, arbitrary 1D/2D/3D wrinkled architectures with microscale features and nanoscale texturing were readily fabricated via point-by-point assembly. It is demonstrated that the wrinkle morphologies can be well produced with an optimal wrinkle wavelength of 40 nm and with a nearly arbitrary structural design in a straightforward and cost-effective way. Multifarious wrinkle structures can be fabricated on demand and flexibly tuned by manipulating the processing parameters, which results in wavelength-controllable nanowrinkled patterns. For future applications, we realized the dynamic transformation of wrinkled cellular microstructures by regulating the stress mismatch from interfacial to structural, which can delaminate and unfold by 140% in response to strain.

Apart from the demonstrated manufacturing designability and practicality, this 3D hierarchical manufacturing technique is still in its infancy, and there will be limitations in terms of the printable area, material applicability, and structural accuracy of the printed pattern (note S4). For the following steps, exploring potential printable materials with a compliant critical response to laser coupling stimuli will enhance the flexibility to print more complicated 3D architectures for promising applications (note S5). From the perspective of experimental improvements, using high-throughput fabrication techniques (*57*) and minimizing postprocessing interferences will boost the productivity and stability of the output morphologies. Meanwhile, the inhomogeneous polymerization induced by a focused Gaussian beam should be considered, combined with the mature core/shell bilayer systems (*32*) and diffusion analytical models (*58*). Furthermore, a deeper theoretical analysis considering real-time energy coupling and potential inhomogeneous distribution will improve the generalizability of this scheme. Overall, this work not only presents a multifunctional platform for sophisticated nanostructured fabrication but also promotes the in-depth investigation of the underlying instability mechanisms, paving the way for developing advanced 3D/4D nanomanufacturing technology.

MATERIALS AND METHODS

Preparation of hydrogel precursor

In a typical procedure, 1 g of NIPAM (97%) was added to 4 ml of PEGDA (Mn 700) and then stirred vigorously. After complete dissolution, 1 ml of the above solution, 2.5 mg of methylene blue (MB; 82%), and 50 μl of EG (99%) were mixed, followed by magnetic stirring for 12 hours to ensure the complete mixing of each component in the solution. Once made, the precursor was kept under yellow light conditions to prevent unnecessary exposure. PEGDA and MB were purchased from Sigma-Aldrich. NIPAM was obtained from TCI Co. Ltd. EG was provided by Alfa Aesar Co. Ltd. All chemicals were directly used as received.

FsLDW fabrication processing

Before fabrication, glass substrates were treated with oxygen plasma at 200 mtorr for 5 min and immersed for 12 hours in a solution composed of 2 ml of 3-(trimethoxysilyl) propyl methacrylate (Sigma-Aldrich), 100 ml of ethanol, and 5 ml of deionized water. After being rinsed in ethanol for 1 hour, the acrylate-functionalized substrate was baked at 90°C for 1 hour, followed by drying in a vacuum and nitrogen purging, and was subsequently served as the printing substrate. For better compatibility with the inverted FsLDW setup and high NA objectives, coverslips (24 mm by 24 mm by 170 μm; Citotest Scientific Co. Ltd.) are used as the glass substrate in this work. In the fabrication procedure, ≈20 μl of aqueous hydrogel precursor was dropped onto a cover glass substrate. The microstructures were fabricated on the glass substrate using a laboratory-built FsLDW system. The laser source of the system is a femtosecond mode–locked Ti:sapphire laser (100 fs of pulse width, 80 MHz of repetition rate; Coherent, Chameleon Discovery) with tunable wavelengths ranging from 680 to 1300 nm, and the central laser wavelength used for FsLDW fabrication was 780 nm. The laser beam was steered by a combination of a 4*f* imaging system and 2D galvo mirrors (SCANLAB,

intelliSCAN III 14), and it was tightly focused within the sample by an oil-immersion objective lens (Olympus; 1.42 NA, ×60). An acousto-optic modulator (AA OPTO-ELECTRONIC, MT110) was used to modulate the beam delivery and output laser power. A piezo stage (Physik Instrument, P-563.3CD) was used to control the vertical scanning movements of the focused laser spot. After fabrication, the laser-written structures were rinsed in isopropyl alcohol for 4 min to remove any unpolymerized prepolymer solution and air-dried in a horizontal orientation in steady air, and the microstructures were obtained on the glass substrate.

Micromechanical characterization

The mechanical properties of the laser-written structures were investigated by a Micromechanical Testing System (FemtoTools, FT-MTA02). An FT-S100000 microforce sensing probe with a force range of ±100,000 μN and a resolution of 5 μN was used with a 50 μm–by–50 μm tip to measure the compression forces of blocks of polymerized hydrogel with dimensions of 100 μm by 100 μm by 20 μm. The adhesive forces between the laser-written structures and the uncoated glass substrates were measured by an FT-S1000-L lateral microforce sensing probe with a force range of ±1000 μN and a resolution of 0.05 μN.

Material and structure characterization

The morphologies of the hydrogel microstructures were characterized using a field-emission scanning electron microscope (FEI Nova NanoSEM 450). A thin layer of Au was sputtered onto samples for better SEM imaging. The 3D surface profiles were measured by a 3D LSCM (Keyence, VK-X1100) and/or an AFM (Bruker, Dimension Edge). The leading functional groups of the hydrogel precursor and photopolymerized microstructure were measured using FTIR (Bruker, VERTEX 70). The optical images and videos were acquired using an Olympus IX83 optical microscope equipped with a charge-coupled device camera.

SUPPLEMENTARY MATERIALS

Supplementary material for this article is available at https://science.org/doi/10.1126/sciadv.abn9942

REFERENCES AND NOTES

1. G. T. Eisenhoffer, P. D. Loftus, M. Yoshigi, H. Otsuna, C.-B. Chien, P. A. Morcos, J. Rosenblatt, Crowding induces live cell extrusion to maintain homeostatic cell numbers in epithelia. *Nature* **484**, 546–549 (2012).
2. W. Miao, S. Zheng, J. Zhou, B. Zhang, R. Fang, D. Hao, L. Sun, D. Wang, Z. Zhu, X. Jin, Y. Tian, L. Jiang, Microchannel and nanofiber array morphology enhanced rapid superspreading on animals' corneas. *Adv. Mater.* **33**, 2007152 (2021).
3. G. F. Striedter, S. Srinivasan, E. S. Monuki, Cortical folding: When, where, how, and why? *Annu. Rev. Neurosci.* **38**, 291–307 (2015).
4. P. Wang, M. Hu, H. Wang, Z. Chen, Y. Feng, J. Wang, W. Ling, Y. Huang, The evolution of flexible electronics: From nature, beyond nature, and to nature. *Adv. Sci.* **7**, 2001116 (2020).
5. X. Hu, Y. Dou, J. Li, Z. Liu, Buckled structures: Fabrication and applications in wearable electronics. *Small* **15**, 1804805 (2019).
6. K. Wu, Y. Sun, H. Yuan, J. Zhang, G. Liu, J. Sun, Harnessing dynamic wrinkling surfaces for smart displays. *Nano Lett.* **20**, 4129–4135 (2020).
7. K. Kim, S.-U. Kim, S. Choi, K. Heo, S. Ahn, J.-H. Na, High-definition optophysical image construction using mosaics of pixelated wrinkles. *Adv. Sci.* **7**, 2002134 (2020).
8. J. S. Bangsund, T. R. Fielitz, T. J. Steiner, K. Shi, J. R. Van Sambeek, C. P. Clark, R. J. Holmes, Formation of aligned periodic patterns during the crystallization of organic semiconductor thin films. *Nat. Mater.* **18**, 725–731 (2019).
9. Y. Rahmawan, C.-M. Chen, S. Yang, Recent advances in wrinkle-based dry adhesion. *Soft Matter* **10**, 5028–5039 (2014).
10. D. H. K. Nguyen, O. Bazaka, K. Bazaka, R. J. Crawford, E. P. Ivanova, Three-dimensional hierarchical wrinkles on polymer films: From chaotic to ordered antimicrobial topographies. *Trends Biotechnol.* **38**, 558–571 (2020).
11. M. Mirbagheri, V. Adibnia, B. R. Hughes, S. D. Waldman, X. Banquy, D. Kun Hwang, Advanced cell culture platforms: A growing quest for emulating natural tissues. *Mater. Horiz.* **6**, 45–71 (2019).
12. Y. Tan, J. Yan, Z. Chu, Thermal-shrinking-induced ring-patterned boron nitride wrinkles on carbon fibers. *Carbon.* **152**, 532–536 (2019).
13. W. Li, Y. Liu, J. Leng, Harnessing wrinkling patterns using shape memory polymer microparticles. *ACS Appl. Mater. Interfaces* **13**, 23074–23080 (2021).
14. C. Xu, G. T. Stiubianu, A. A. Gorodetsky, Adaptive infrared-reflecting systems inspired by cephalopods. *Science* **359**, 1495–1500 (2018).
15. K. S. Tiaw, S. H. Teoh, R. Chen, M. H. Hong, Processing methods of ultrathin poly(ε-caprolactone) films for tissue engineering applications. *Biomacromolecules* **8**, 807–816 (2007).
16. M. Yunusa, G. J. Amador, D.-M. Drotlef, M. Sitti, Wrinkling instability and adhesion of a highly bendable gallium oxide nanofilm encapsulating a liquid-gallium droplet. *Nano Lett.* **18**, 2498–2504 (2018).
17. Y. Yang, H.-H. Dai, F. Xu, M. Potier-Ferry, Pattern transitions in a soft cylindrical shell. *Phys. Rev. Lett.* **120**, 215503 (2018).
18. H. S. Kim, A. J. Crosby, Solvent-responsive surface via wrinkling instability. *Adv. Mater.* **23**, 4188–4192 (2011).
19. J. Y. Chung, A. J. Nolte, C. M. Stafford, Diffusion-controlled, self-organized growth of symmetric wrinkling patterns. *Adv. Mater.* **21**, 1358–1362 (2009).
20. T. Ma, T. Li, L. Zhou, X. Ma, J. Yin, X. Jiang, Dynamic wrinkling pattern exhibiting tunable fluorescence for anti-counterfeiting applications. *Nat. Commun.* **11**, 1811 (2020).
21. H. J. Bae, S. Bae, C. Park, S. Han, J. Kim, L. N. Kim, K. Kim, S.-H. Song, W. Park, S. Kwon, Biomimetic microfingerprints for anti-counterfeiting strategies. *Adv. Mater.* **27**, 2083–2089 (2015).
22. Z. Wen, Y. Yang, N. Sun, G. Li, Y. Liu, C. Chen, J. Shi, L. Xie, H. Jiang, D. Bao, Q. Zhuo, X. Sun, A Wrinkled PEDOT:PSS film based stretchable and transparent triboelectric nanogenerator for wearable energy harvesters and active motion sensors. *Adv. Funct. Mater.* **28**, 1803684 (2018).
23. M. Wang, Y. Qiu, J. Jia, C. Wang, J. Deng, K. Pan, Wavelength-gradient graphene films for pressure-sensitive sensors. *Adv. Mater. Technol.* **4**, 1800363 (2019).
24. M. R. Aufan, Y. Sumi, S. Kim, J. Y. Lee, Facile synthesis of conductive polypyrrole wrinkle topographies on polydimethylsiloxane via a swelling–deswelling process and their potential uses in tissue engineering. *ACS Appl. Mater. Interfaces* **7**, 23454–23463 (2015).
25. A. Korolj, C. Laschinger, C. James, E. Hu, C. Velikonja, N. Smith, I. Gu, S. Ahadian, R. Willette, M. Radisic, B. Zhang, Curvature facilitates podocyte culture in a biomimetic platform. *Lab Chip* **18**, 3112–3128 (2018).
26. Z. Jin, Y. Li, K. Yu, L. Liu, J. Fu, X. Yao, A. Zhang, Y. He, 3D printing of physical organ models: Recent developments and challenges. *Adv. Sci.* **8**, 2101394 (2021).
27. G. Liu, X. Zhang, X. Chen, Y. He, L. Cheng, M. Huo, J. Yin, F. Hao, S. Chen, P. Wang, S. Yi, L. Wan, Z. Mao, Z. Chen, X. Wang, Z. Cao, J. Lu, Additive manufacturing of structural materials. *Mater. Sci. Eng. R Rep.* **145**, 100596 (2021).
28. M. S. S. Bharati, V. R. Soma, Flexible SERS substrates for hazardous materials detection: Recent advances. *Opto-Electron. Adv.* **4**, 210048 (2021).
29. X. Tang, W. Yang, S. Yin, G. Tai, M. Su, J. Yang, H. Shi, D. Wei, J. Yang, Controllable graphene wrinkle for a high-performance flexible pressure sensor. *ACS Appl. Mater. Interfaces* **13**, 20448–20458 (2021).
30. Y. Pang, Y. Cao, Y. Chu, M. Liu, K. Snyder, D. MacKenzie, C. Cao, Additive manufacturing of batteries. *Adv. Funct. Mater.* **30**, 1906244 (2020).
31. D. Guo, Y. Lu, Overview of extreme manufacturing. *Int. J. Extreme Manuf.* **1**, 020201 (2019).
32. Y. Tan, B. Hu, J. Song, Z. Chu, W. Wu, Bioinspired multiscale wrinkling patterns on curved substrates: An overview. *Nano-Micro Lett.* **12**, 101 (2020).
33. H. Yuan, K. Wu, J. Zhang, Y. Wang, G. Liu, J. Sun, Curvature-controlled wrinkling surfaces for friction. *Adv. Mater.* **31**, 1900933 (2019).
34. J. Song, Y. Tan, Z. Chu, M. Xiao, G. Li, Z. Jiang, J. Wang, T. Hu, Hierarchical reduced graphene oxide ridges for stretchable, wearable, and washable strain sensors. *ACS Appl. Mater. Interfaces* **11**, 1283–1293 (2019).
35. H. J. Bae, S. Bae, J. Yoon, C. Park, K. Kim, S. Kwon, W. Park, Self-organization of maze-like structures via guided wrinkling. *Sci. Adv.* **3**, e1700071 (2017).
36. H. R. Zhang, F. Yang, J. Dong, L. Du, C. Wang, J. Zhang, C. F. Guo, Q. Liu, Kaleidoscopic imaging patterns of complex structures fabricated by laser-induced deformation. *Nat. Commun.* **7**, 13743 (2016).
37. Y. Zhang, Y. Jiao, C. Li, C. Chen, J. Li, Y. Hu, D. Wu, J. Chu, Bioinspired micro/nanostructured surfaces prepared by femtosecond laser direct writing for multifunctional applications. *Int. J. Extreme Manuf.* **2**, 032002 (2020).
38. L. Zhou, K. Hu, W. Zhang, G. Meng, J. Yin, X. Jiang, Regulating surface wrinkles using light. *Natl. Sci. Rev.* **7**, 1247–1257 (2020).

39. M. Li, N. Hakimi, R. Perez, S. Waldman, J. A. Kozinski, D. K. Hwang, Microarchitecture for a three-dimensional wrinkled surface platform. *Adv. Mater.* **27**, 1880–1886 (2015).
40. L. Ma, L. He, Y. Ni, Tunable hierarchical wrinkling: From models to applications. *J. Appl. Phys.* **127**, 111101 (2020).
41. J. Fischer, M. Wegener, Three-dimensional optical laser lithography beyond the diffraction limit. *Laser Photonics Rev.* **7**, 22–44 (2013).
42. K. Sugioka, Hybrid femtosecond laser three-dimensional micro-and nanoprocessing: A review. *Int. J. Extreme Manuf.* **1**, 012003 (2019).
43. Y. Jia, S. Wang, F. Chen, Femtosecond laser direct writing of flexibly configured waveguide geometries in optical crystals: Fabrication and application. *Opto-Electron. Adv.* **3**, 190042–190012 (2020).
44. Z. Lin, H. Liu, L. Ji, W. Lin, M. Hong, Realization of ~10 nm features on semiconductor surfaces via femtosecond laser direct patterning in far field and in ambient air. *Nano Lett.* **20**, 4947–4952 (2020).
45. O. Kuksenok, A. C. Balazs, Modeling the photoinduced reconfiguration and directed motion of polymer gels. *Adv. Funct. Mater.* **23**, 4601–4610 (2013).
46. E. Lee, B. Sun, J. Luo, S. Singh, D. Choudhury, D. Yong, X. Yu, Q. Wang, Compact pulsed thulium-doped fiber laser for topographical patterning of hydrogels. *Opto-Electron. Adv.* **3**, 190039 (2020).
47. D.-X. Liu, Y.-L. Sun, W.-F. Dong, R.-Z. Yang, Q.-D. Chen, H.-B. Sun, Dynamic laser prototyping for biomimetic nanofabrication. *Laser Photonics Rev.* **8**, 882–888 (2014).
48. A. Halperin, M. Kröger, F. M. Winnik, Poly(N-isopropylacrylamide) phase diagrams: Fifty years of research. *Angew. Chem. Int. Ed.* **54**, 15342–15367 (2015).
49. X. Sun, M. J. Hourwitz, E. M. Baker, B. U. S. Schmidt, W. Losert, J. T. Fourkas, Replication of biocompatible, nanotopographic surfaces. *Sci. Rep.* **8**, 564 (2018).
50. M. G. Guney, G. K. Fedder, Estimation of line dimensions in 3D direct laser writing lithography. *J. Micromechanics Microengineering.* **26**, 105011 (2016).
51. J. Bauer, A. Guell Izard, Y. Zhang, T. Baldacchini, L. Valdevit, Programmable mechanical properties of two-photon polymerized materials: From nanowires to bulk. *Adv. Mater. Technol.* **4**, 1900146 (2019).
52. M. Liu, S. Wang, L. Jiang, Nature-inspired superwettability systems. *Nat. Rev. Mater.* **2**, 1–17 (2017).
53. C. Huang, Z. Wang, D. Quinn, S. Suresh, K. J. Hsia, Differential growth and shape formation in plant organs. *Proc. Natl. Acad. Sci. U.S.A.* **115**, 12359–12364 (2018).
54. F. Brau, P. Damman, H. Diamant, T. A. Witten, Wrinkle to fold transition: Influence of the substrate response. *Soft Matter* **9**, 8177–8186 (2013).
55. S. H. Kang, S. Shan, W. L. Noorduin, M. Khan, J. Aizenberg, K. Bertoldi, Buckling-induced reversible symmetry breaking and amplification of chirality using supported cellular structures. *Adv. Mater.* **25**, 3380–3385 (2013).
56. S. Li, B. Deng, A. Grinthal, A. Schneider-Yamamura, J. Kang, R. S. Martens, C. T. Zhang, J. Li, S. Yu, K. Bertoldi, J. Aizenberg, Liquid-induced topological transformations of cellular microstructures. *Nature* **592**, 386–391 (2021).
57. V. Hahn, P. Kiefer, T. Frenzel, J. Qu, E. Blasco, C. Barner-Kowollik, M. Wegener, Rapid assembly of small materials building blocks (Voxels) into large functional 3D metamaterials. *Adv. Funct. Mater.* **30**, 1907795 (2020).
58. Z. Wu, N. Bouklas, R. Huang, Swell-induced surface instability of hydrogel layers with material properties varying in thickness direction. *Int. J. Solids Struct.* **50**, 578–587 (2013).
59. M. Hippler, E. Blasco, J. Qu, M. Tanaka, C. Barner-Kowollik, M. Wegener, M. Bastmeyer, Controlling the shape of 3D microstructures by temperature and light. *Nat. Commun.* **10**, 232 (2019).
60. A. Vogel, J. Noack, G. Hüttman, G. Paltauf, Mechanisms of femtosecond laser nanosurgery of cells and tissues. *Appl. Phys. B.* **81**, 1015–1047 (2005).
61. A. Vogel, N. Linz, S. Freidank, G. Paltauf, Femtosecond-laser-induced nanocavitation in water: Implications for optical breakdown threshold and cell surgery. *Phys. Rev. Lett.* **100**, 038102 (2008).
62. Y.-L. Sun, Q. Li, S.-M. Sun, J.-C. Huang, B.-Y. Zheng, Q.-D. Chen, Z.-Z. Shao, H.-B. Sun, Aqueous multiphoton lithography with multifunctional silk-centred bio-resists. *Nat. Commun.* **6**, 8612 (2015).
63. M. A. Biot, Surface instability of rubber in compression. *Appl. Sci. Res. Sect. A.* **12**, 168–182 (1963).
64. T. Tanaka, S.-T. Sun, Y. Hirokawa, S. Katayama, J. Kucera, Y. Hirose, T. Amiya, Mechanical instability of gels at the phase transition. *Nature* **325**, 796–798 (1987).
65. J. Dervaux, M. B. Amar, Mechanical instabilities of gels. *Annu. Rev. Condens. Matter Phys.* **3**, 311–332 (2012).
66. C.-Y. Liaw, J. Pereyra, M. Guvendiren, Wrinkling on covalently anchored hydrogels, in *Wrinkled Polymer Surfaces: Strategies, Methods and Applications*, C. M. González-Henríquez, J. Rodríguez-Hernández, Eds. (Springer International Publishing, 2019), pp. 205–227.
67. W. Hong, Z. Liu, Z. Suo, Inhomogeneous swelling of a gel in equilibrium with a solvent and mechanical load. *Int. J. Solids Struct.* **46**, 3282–3289 (2009).
68. M. K. Kang, R. Huang, Swell-induced surface instability of confined hydrogel layers on substrates. *J. Mech. Phys. Solids* **58**, 1582–1598 (2010).
69. S. Sriram, E. Polukhov, M.-A. Keip, Transient stability analysis of composite hydrogel structures based on a minimization-type variational formulation. *Int. J. Solids Struct.* **230–231**, 111080 (2021).
70. A. D. Drozdov, Mechanical behavior of temperature-sensitive gels under equilibrium and transient swelling. *Int. J. Eng. Sci.* **128**, 79–100 (2018).
71. S. J. D. Jr, R. Scott Cates, P. George Stroot, R. Toomey, Swelling-induced instabilities in microscale, surface-confined poly(N-isopropylacryamide) hydrogels. *Soft Matter* **6**, 3876–3882 (2010).
72. M. K. Kang, R. Huang, Swelling-induced instability of substrate-attached hydrogel lines. *Int. J. Appl. Mech.* **3**, 219–233 (2011).
73. A. Münchinger, V. Hahn, D. Beutel, S. Woska, J. Monti, C. Rockstuhl, E. Blasco, M. Wegener, Multi-photon 4D printing of complex liquid crystalline microstructures by in situ alignment using electric fields. *Adv. Mater. Technol.* **7**, 2100944 (2021).
74. I. D. Bellis, S. Nocentini, M. G. D. Santi, D. Martella, C. Parmeggiani, S. Zanotto, D. S. Wiersma, Two-photon laser writing of soft responsive polymers via temperature-controlled polymerization. *Laser Photonics Rev.* **15**, 2100090 (2021).

Acknowledgments: We thank the Analytical and Testing Center of HUST, the facility support of the Center for Nanoscale Characterization and Devices at Wuhan National Laboratory for Optoelectronics, and the technical support by the Experiment Center for Advanced Manufacturing and Technology in School of Mechanical Science and Engineering of HUST. We appreciate the efforts of all medical workers and volunteers around the world who are fighting against the coronavirus disease 2019 pandemic. We also thank the support from our families and friends during the isolation period. **Funding:** This work was funded by the National Key Research and Development Program of China (grant 2021YFF0502700), Innovation project of Optics Valley Laboratory (grant OVL2021ZD002), and China Postdoctoral Science Foundation (grant 2019M662597). **Author contributions:** Conceptualization: X.F. and W.X. Methodology: X.F., C.D., and F.C. Investigation: X.F., B.J., and Y.L. Visualization: X.F. and H.G. Supervision: W.X., H.G., and L.D. Writing—original draft: X.F. and H.G. Writing—review and editing: W.X., X.F., and H.G. **Competing interests:** X.F., C.D., H.G., B.J., Y.L., F.C., L.D., and W.X. are inventors on a patent application related to this work filed by Huazhong University of Science and Technology (no. 202210396910.0, filed 15 April 2022). The authors declare that they have no other competing interests. **Data and materials availability:** All data needed to evaluate the conclusions in the paper are present in the paper and/or the Supplementary Materials.

Submitted 6 January 2022
Accepted 27 June 2022
Published 10 August 2022
10.1126/sciadv.abn9942